minerals

Article

Strain Energy Release and Deep Rock Failure Due to Excavation in Pre-Stressed Rock

Peng Xiao, Diyuan Li * and Quanqi Zhu

School of Resources and Safety Engineering, Central South University, Changsha 410083, China; xiaopengaizhanghuimin@csu.edu.cn (P.X.); quanqi_zhu@csu.edu.cn (Q.Z.)
* Correspondence: diyuan.li@csu.edu.cn

Abstract: Deep rock engineering is in a high pre-stressed state before excavation. In this research, a method to calculate the release of strain energy caused by excavation in pre-stressed rock is proposed. The normal stress release after excavation leads to a reduction in strain energy in rock specimens. The influence of excavation height and width on strain energy release is inconsistent under vertical loading. When the height of the hole is 1 mm, the strain energy release is large, and the increase in height of hole leads to a slow increase in the strain energy release. When the width of the hole is 1 mm, the strain energy release is very small, and the increase in the width of the hole leads to an increasingly faster release of strain energy. This strain energy release exponentially increases with the increase in the lateral pressure coefficient, showing a trend in the second power of the lateral pressure coefficient. Moreover, the tunnel failure caused by excavation under high stress is obtained by a numerical calculation. The failure modes of the deep tunnel model are strain rockbursts caused by tangential stress concentrations and spalling caused by normal stress release, which is also observed in the failure mode of the actual tunnel.

Keywords: deep engineering; tunnel excavation; high ground stress; strain energy release; rockburst

Citation: Xiao, P.; Li, D.; Zhu, Q. Strain Energy Release and Deep Rock Failure Due to Excavation in Pre-Stressed Rock. *Minerals* **2022**, *12*, 488. https://doi.org/10.3390/min12040488

Academic Editor: Yosoon Choi

Received: 24 March 2022
Accepted: 14 April 2022
Published: 16 April 2022

1. Introduction

With the large-scale development of deep underground projects, such as deep mines [1,2], deep buried traffic tunnels [3,4], and hydropower station chambers [5,6], many ground pressure disasters have been reported in deep projects [7–9]. Therefore, the study of deep ground pressure disasters has become a popular topic in the field of rock engineering [10]. Many disasters often occur in deep engineering, such as rockbursts, slabbing, large-scale collapse and large deformation [11–13]. Many scholars explain the mechanism of these disasters from many aspects, such as in situ stress [14,15], strength theory [16–18], rock fault [19,20], the energy storage of rock [21,22], engineering structure [23,24], dynamic disturbance [25–28], stress monitoring [29], and so on [30–34]. Among them, the high ground stress is one of the most important causes of ground pressure disasters. Many studies show that most ground pressure disasters occur in high-stress areas [18,35,36].

In the study of the influence of ground stress on ground pressure disasters, Hu and Gong et al. found that the tangential stress concentration after excavation led to spalling and rockburst through the true triaxial testing of specimens with holes [37–39]. Tao et al. found that the release of normal stress on the free face after excavation caused damage to rock through numerical simulation [40–42]. Many engineering practices show that a faster excavation speed leads to more serious surrounding rock damage [43]. This is because the faster the excavation results, the faster the release of normal stress on the excavation surface. Therefore, the normal stress release on the excavation surface of surrounding rock by excavation needs to be considered.

Su et al. found that the excavation in high-stressed rock mass led to the release of radial stress and the concentration of tangential stress [44]. Considering the initial stress state, there are some differences between the excavation after loading and the loading after excavation. For the loading after excavation, e.g., the laboratory test of a rock specimen with holes, there is no release of normal stress during the loading process, since there is no normal stress around the holes to begin with. For excavation after loading, it is more suitable to describe the complete process of deep engineering excavations. As shown in Figure 1, normal stress exists around the roadway before excavation, and excavation will lead to the release of normal stress around the roadway and the concentration of tangential stress.

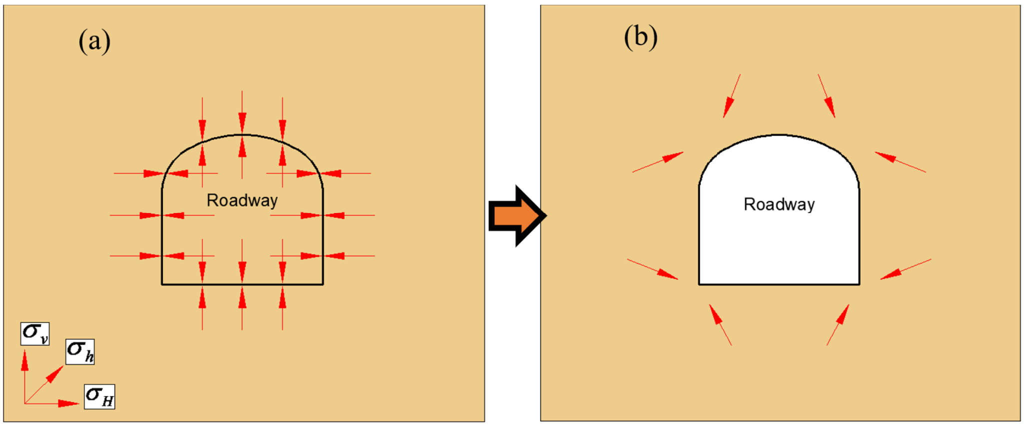

Figure 1. The stress field evolution caused by excavation in deep engineering. (**a**) Stress state before excavation. (**b**) Release of normal stress and concentration of tangential stress after excavation.

It is important to calculate the released strain energy after excavation, which can provide an important basis for energy absorption support and rockburst prediction. At present, there are relatively few studies on the normal stress release caused by excavation in deep pre-stressed rock. The tests of excavation in pre-stressed rock are difficult in the laboratory. This research proposes a method to calculate the strain energy release caused by excavation. The released strain energy caused by excavation in pre-stressed rock is calculated through laboratory tests and numerical calculations. Moreover, the influence of excavation height, width and lateral pressure on the strain energy release are analyzed. Finally, the deep tunnel failure due to excavation in pre-stressed rock is reproduced by means of a numerical simulation.

2. Calculation of Strain Energy Release by Excavation in Pre-Stressed Rock

2.1. Methodology

It is difficult to measure the released strain energy directly caused by excavation, but it can be indirectly obtained by another way. As shown in Figure 2, the intact specimen and the specimen with holes are compressed by a test machine and subjected to the same deformation l_0, except that the second specimen includes a hole of size $w \times h$, the size of the two specimens is the same: W is width of specimen, H is height, T is thickness, F is external load, l is displacement of load, w is the width of hole, and h is the height of hole.

During loading, the strain energy is stored inside the two specimens. In this paper, the U_{Int} represents the strain energy of the intact specimen, which is calculated by Equation (1); U_{Hole} represents the strain energy of the hole, which is calculated by Equation (2); $U_{Aft\text{-}ex}$ represents the strain energy of the specimen after excavation, which is calculated by Equation (3); and $U_{Spe\text{-}ho}$ represents the strain energy of the specimen with a hole, which is calculated by Equation (4). Due to the same deformation of the two specimens, the stress state of the intact specimen after excavating a hole will eventually be the same as that of the specimen with a hole. If the $U_{Aft\text{-}ex}$ and $U_{Spe\text{-}ho}$ are equal, there is no strain energy release after excavation; otherwise, there is a strain energy release after excavation. The actual released strain energy U_{Rele} can be calculated by Equation (5):

$$U_{Int} = \int_0^{l_0} F_1 dl \tag{1}$$

$$U_{Hole} = \frac{hw}{HW} U_{Int} \tag{2}$$

$$U_{Aft-ex} = U_{Int} - U_{Hole} \tag{3}$$

$$U_{Spe-ho} = \int_0^{l_0} F_2 dl \tag{4}$$

$$U_{Rele} = U_{Int} - U_{Hole} - U_{Spe-ho} \tag{5}$$

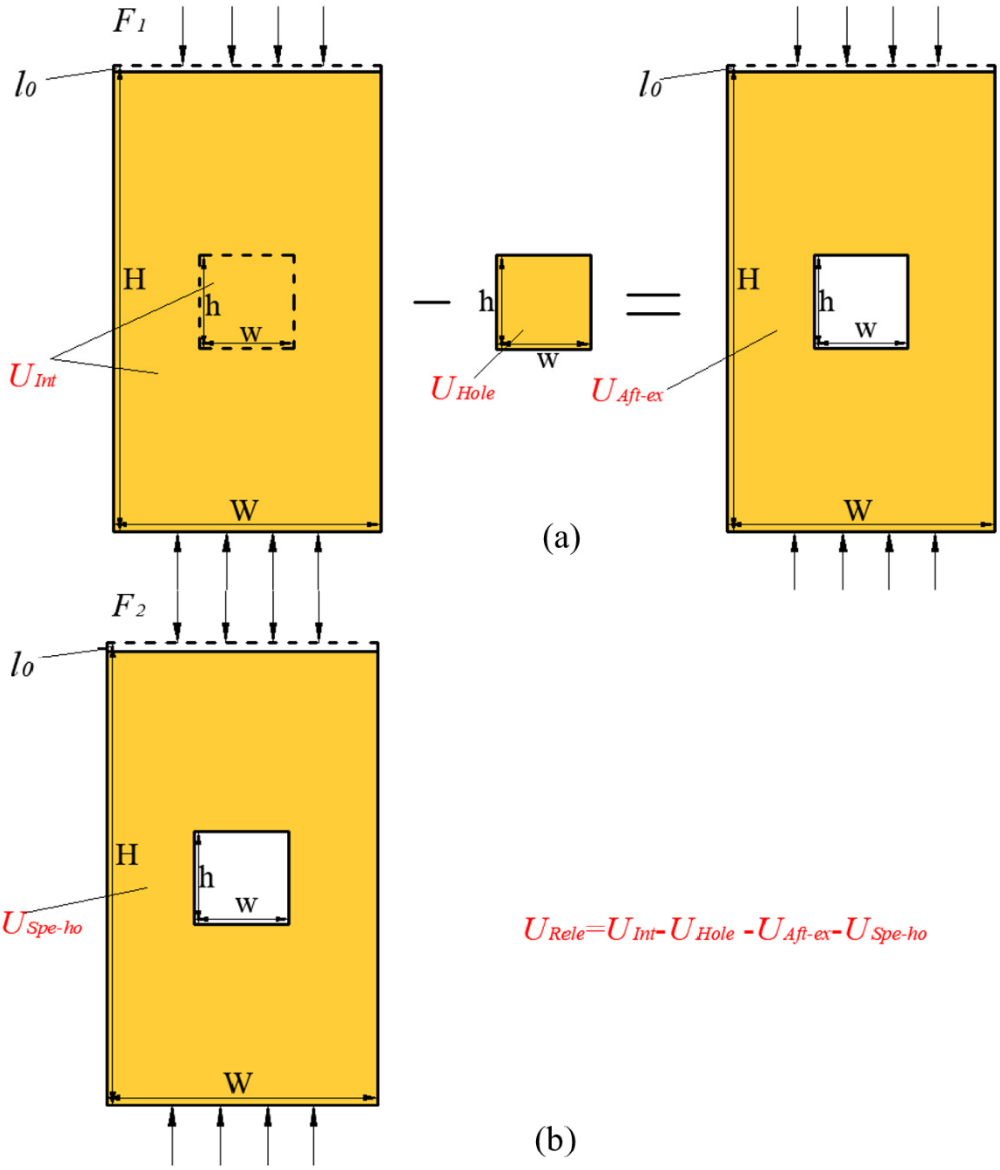

Figure 2. The intact specimen and specimen with a hole under the same compression deformation l_0. (**a**). Excavation of hole after a certain deformation l_0. (**b**). A certain deformation l_0 after excavation of hole.

2.2. Strain Energy Release by Excavation in Laboratory Test

As shown in Figure 3, the specimen is marble, its size is 150 mm × 120 mm × 20 mm ($H \times W \times T$), and a rectangular hole is prefabricated in the geometric center of specimen. In order to ensure the integrity and homogeneity of specimen, a whole marble plate was selected for processing, and the surface of specimen was smooth without obvious defects visible to the naked eye. The rectangular hole was made by professional water jet cutting mechanical equipment OMAX 2626. There are two types of specimens: intact specimen (S-Intact) and specimen with rectangle hole (S-Hole). The specimen sizes are shown in Table 1. Instron-1346 hydraulic servo control testing machine was used for uniaxial compression test. The loading strain rate was 2×10^{-5}, which belonged to quasi-static loading. The loading curve with deformation was selected as 0.453 mm, equivalent to 0.3% strain to ensure that all specimens were always in elastic stage. The load versus displacement curves of two specimens are shown in Figure 4. On the whole, the stress–strain curves of two specimens showed the characteristics of plastic elastic deformation.

Table 1. The size of specimen and hole.

Specimens	High/mm	Width/mm	Thick/mm	Hole Size/mm
S-Intact	149.7	119.1	21.0	0
S-Hole	149.3	119.2	21.6	22 × 22

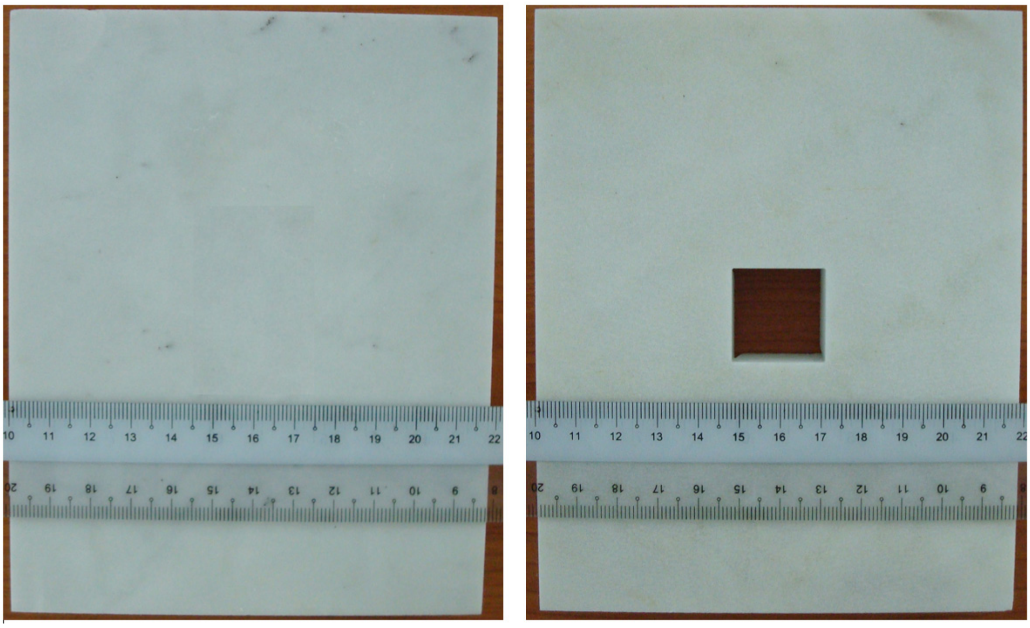

Figure 3. Intact specimen and specimen with rectangle hole.

The strain energy of each part was calculated, as shown in Figure 4 and Equations (1)–(5); the strain energy of each part is shown in Table 2. If the stored energy in the hole is subtracted, is the residual strain energy of intact specimen equal to the strain energy of specimen with hole? It can be seen from Table 2 that the residual strain energy $U_{Aft\text{-}ex}$ of the intact specimen after excavating the hole is greater than that $U_{Spe\text{-}ho}$ of the specimen with the hole. Since the stress state of the intact specimen after excavating the hole will eventually be same as that of the specimen with hole, this indicates that there is strain energy release around the hole after excavation. The actual released strain energy U_{Rele} can be calculated by U_{Int}-U_{Hole}-$U_{Spe\text{-}ho}$.

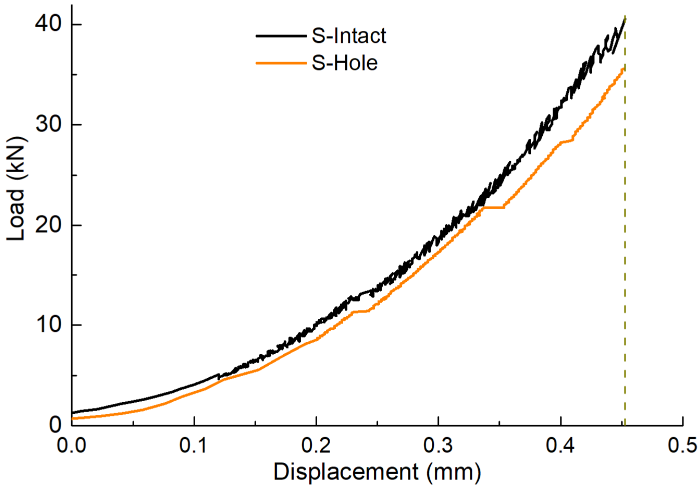

Figure 4. Load versus displacement curve of four specimens.

Table 2. The strain energy of each part.

Specimen	U_{Int}/J	U_{Hole}/J	$U_{Aft\text{-}ex}$/J	$U_{Spe\text{-}ho}$/J	U_{Rele}/J
S-Intact	6.848	0.184	6.664	---	0.703
S-Hole	---	---	---	5.961	

The strain energy change in the intact specimen from loading to excavation and then to stability (stress balance) is shown in Figure 5; points 1 to 2 represent the gradual increase in strain energy during loading of intact specimen. Point 2 represents stop loading. Point 3 represents the residual strain energy $U_{Aft\text{-}ex}$ of intact specimen after excavating hole, the stress around hole is not balanced. Point 4 represents the equilibrium state after the normal stress around the hole is released and the tangential stress is concentrated. It can be seen from Figure 5 that the strain energy of intact specimen gradually decreases from point 2 to point 3 and then to point 4. This also means that the deep pre-stressed rock changes from the stable state before excavation to the unstable state after excavation, and finally to the stable state.

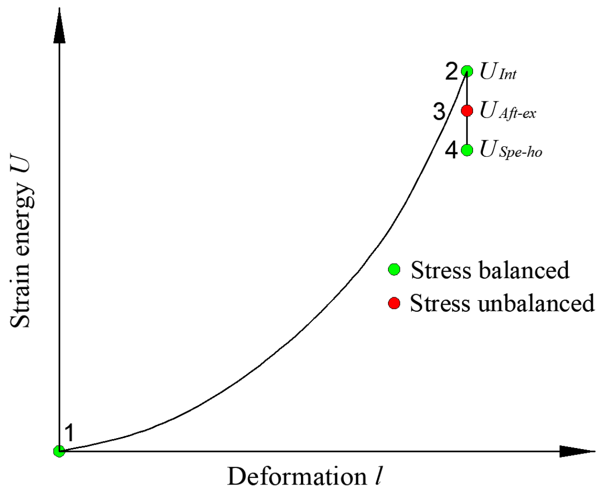

Figure 5. Strain energy change in specimen at different stages.

2.3. *Strain Energy Release by Excavation in Numerical Analysis*

As shown in Figure 6, two elastic material models were built in a code ELFEN. The height H of specimen is 150 mm, width W is 120 mm, thickness T is 20 mm, and the size of hole is the same as that in Section 2. In order to obtain a more obvious law of strain energy release under different states, the model was set to elastic, and no failure criterion was adopted in the model, which means that plastic deformation and failure did not occur. The model properties are shown in Table 3. The elastic modulus of the specimen was obtained from the load displacement curve of the intact specimen in Figure 4, which was about 5.01 GPa. The specimen was placed between two pressure platens. The loading rate was about 6.7×10^{-3} s^{-1}, which could be considered as a quasi-static loading. When the displacement of the pressure platen reached 0.453 mm, the loading ended.

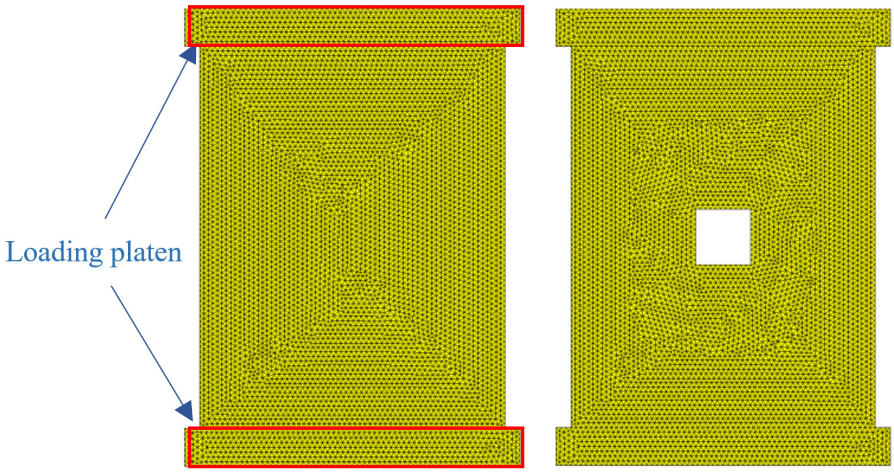

Figure 6. Two models of intact specimen and specimen with rectangle hole.

Table 3. Material properties adopted in model.

Mechanical Parameters	Specimen	Loading Platen
Young's modulus (E, GPa)	5.01	211
Poisson's ratio (ν)	0.33	0.29
Density (ρ, kg/m^3)	2700	7840
Normal penalty (P_n, N/mm^2)	5010	211,000
Tangential penalty (P_t, N/mm^2)	501	21,100
Friction (γ)	0	0
Mesh element size (mm)	2	2
Contact type	Node edge	Node edge

The load versus displacement curve of the two specimens is shown in Figure 7. On the whole, the stress–strain curves of two specimens show the characteristics of elastic deformation. The strain energy of each part was calculated, as shown in Figure 7 and Equations (1)–(5); the strain energy of each part is shown in Table 4. Because there is no initial compaction stage, a specimen of the elastic materials accumulates more strain energy than elastic–plastic materials under the same displacement. The residual strain energy of the intact specimen after excavating the hole was still greater than that of specimen with hole. This showed that the excavation in pre-stressed elastic materials also led to the release of strain energy.

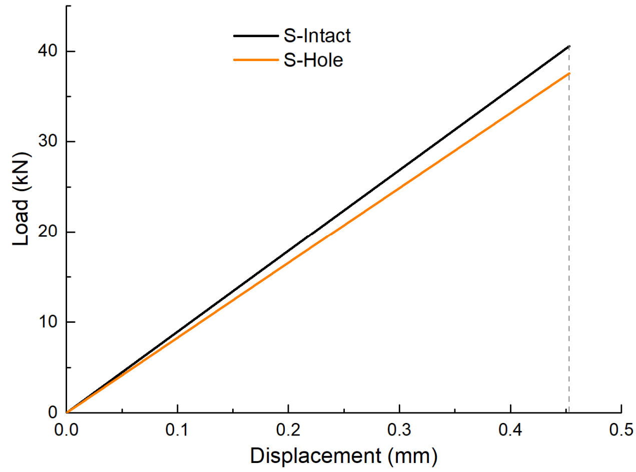

Figure 7. Load versus displacement curve of two models.

Table 4. The strain energy of each part.

Specimen	Displacement/mm	Load/kN	U_{Int}/J	U_{Hole}/J	$U_{Aft\text{-}ex}$/J	$U_{Spe\text{-}ho}$/J	U_{Rele}/J
S-Intact	0.453	40.56	9.186	0.247	8.939	---	0.434
S-Hole		37.55	---	---	---	8.505	

3. Effect of Excavation Height and Width on Strain Energy Release

3.1. Effect of Excavation Height

Through the previous analysis, it was found that excavating holes in pre-stressed rock led to the release of the strain energy of the specimen. In this section, the influence of height *h* of rectangle hole on energy release is analyzed. As shown in Figure 8, if the width of 22 mm is unchanged, the height of rectangle hole gradually changes from 1 mm to 22 mm. The specimen size, loading method and material parameters are consistent with Section 2.3. The common tunnel section size in some deep mines is about 4.5 m × 4.3 m, the maximum size of the hole in the test is 22 mm × 22 mm, and the scale of the test to the real condition is 1:200.

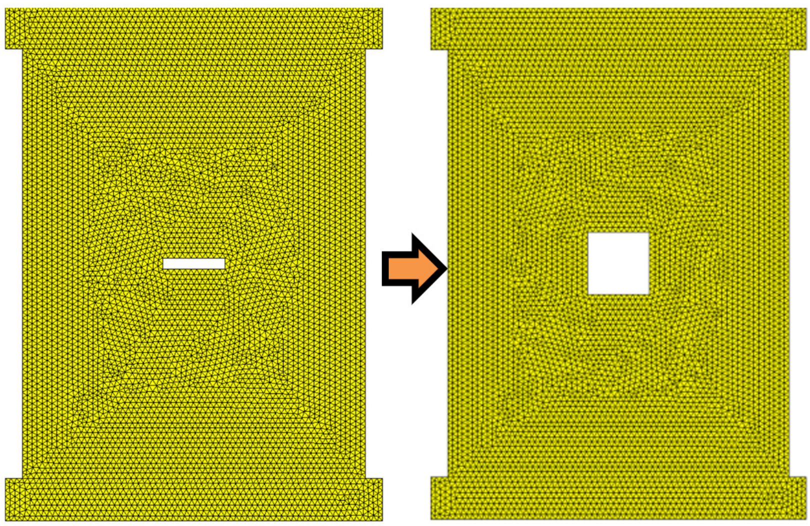

Figure 8. The height *h* of hole increases from 1 mm to 22 mm.

Table 5 shows the load of specimens with holes that have different height and strain energy in each part. Figure 9 is the strain energy release caused by different heights h of holes. With the increase in height *h*, the load of the specimen with holes under the same displacement gradually decreases. When the height of hole is 1 mm, the strain energy release is large. In addition, the increase in height h will lead to the slow increase in strain energy release.

Table 5. The load of specimens with holes that have different height and strain energy in each part.

h/mm	Displacement/mm	Load/kN	U_{Int}/J	U_{Hole}/J	$U_{Aft\text{-}ex}$/J	$U_{Spe\text{-}ho}$/J	U_{Rele}/J
0	0.453	40.56	9.186	---	---	---	0
1		39.10		0.011	9.175	8.856	0.319
4		38.81		0.045	9.141	8.791	0.350
8		38.46		0.090	9.096	8.712	0.384
12		38.18		0.135	9.051	8.648	0.403
16		37.92		0.180	9.007	8.590	0.417
22		37.55		0.247	8.939	8.504	0.435

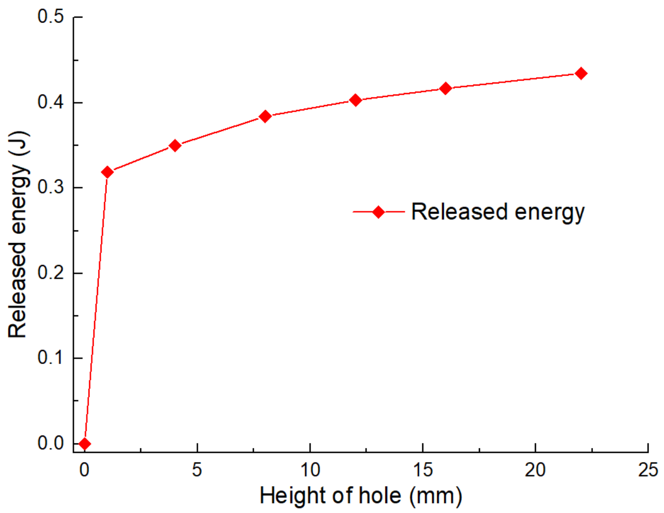

Figure 9. Strain energy release caused by different heights h of excavation holes.

3.2. Effect of Excavation Width

In addition to the excavation height, the influence of excavation width w on strain energy release is analyzed. As shown in Figure 10, if the height of 22 mm remains unchanged, then the width of hole gradually changes from 1 mm to 22 mm. The specimen size, loading method and material parameters are consistent with Section 2.3.

Table 6 is the load of specimens with holes that have different height and strain energy in each part. Figure 11 is the strain energy release caused by different heights h of hole. With the increase in the width of the hole, the load of the specimen with holes under the same displacement gradually decreases. When the width of the hole is 1 mm, the released strain energy is very small, and the increase in the width of the hole will lead to an increasing release of strain energy.

Table 6. The strain energy of each part.

w/mm	Displacement/mm	Load/kN	U_{Int}/J	U_{Hole}/J	$U_{Aft\text{-}ex}$/J	$U_{Spe\text{-}ho}$/J	U_{Rele}/J
0	0.453	40.56	9.186	---	---	---	0
1		40.49		0.011	9.175	9.172	0.003
4		40.31		0.045	9.141	9.129	0.012
8		39.90		0.090	9.096	9.038	0.058
12		39.37		0.135	9.051	8.918	0.133
16		38.73		0.180	9.007	8.772	0.234
22		37.55		0.247	8.939	8.504	0.435

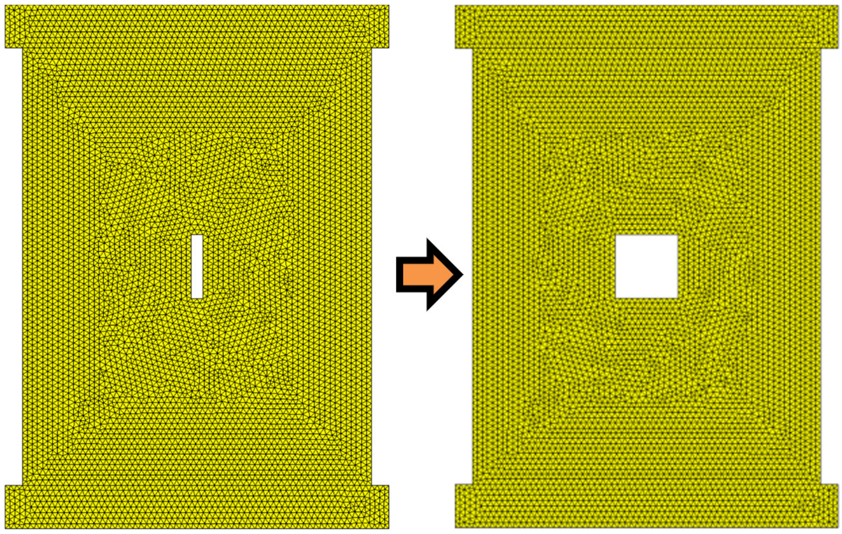

Figure 10. The width of hole w increases from 1 mm to 22 mm.

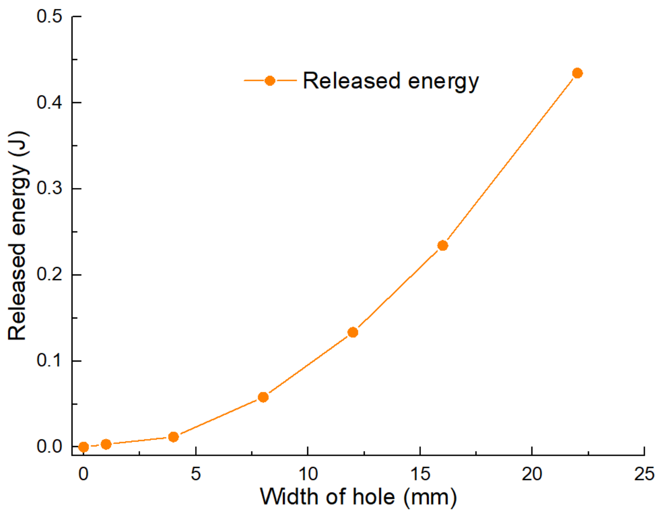

Figure 11. Strain energy release caused by different width w of excavation hole.

3.3. Equation for Released Strain Energy Caused by Excavation

In previous studies, it is mentioned that the excavation of a hole in pre-stressed rock will lead to strain energy release. The strain energy release per unit thickness is given by Equation (6) [18]:

$$U_e = \frac{\pi \sigma^2 A^2}{4E} \tag{6}$$

Considering the specimen thickness, the released strain energy caused by holes is calculated by Equation (7). The maximum principal stress of the intact model in Table 6 is 16.9 MPa, T is 20 mm, E is 5.01 GPa. When the width w of hole is 22 mm, the theoretical value of strain energy release can be calculated as 0.433 J according to Equation (8), which is very close to 0.435 J in Table 6, indicating that Equation (7) is reliable:

$$U_{Rele} = \frac{\pi \sigma^2 w^2 T}{4E} \tag{7}$$

$$U_{Rele} = \frac{\pi \times 16.9^2 \times 10^{12} \times 22^2 \times 20 \times 10^{-9}}{4 \times 5.01 \times 10^9} = 0.433 \text{ J} \tag{8}$$

Combined with Figures 9 and 11, the strain energy releases caused by different height and width of holes are shown in Figure 12. When the size of height or width is less than 16 mm, the strain energy release caused by height and width is very different. When the height and width reach 22 mm, the shapes of the two holes are square with the same side length, and the released strain energy is the same.

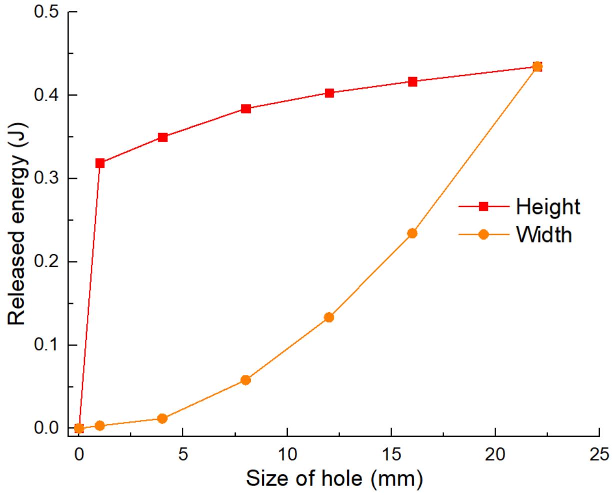

Figure 12. Strain energy release caused by different height and width of excavation holes.

Since the strain energy release is discontinuous when the height of the hole is from 0 to 1 mm, the part from 1 mm to 22 mm is considered, which can represent holes with various height width ratio. Considering the influence of hole height, Equation (9) is obtained by modifying Equation (7). As shown in Figure 13, the fitting accuracy is high. The theoretical value of strain energy release caused by height and width of holes can be calculated by Equation (9):

$$U_{Rele} = \frac{\pi \sigma^2 w^2 T}{4E}(0.78 + 0.22\frac{h}{w}) \quad (9)$$

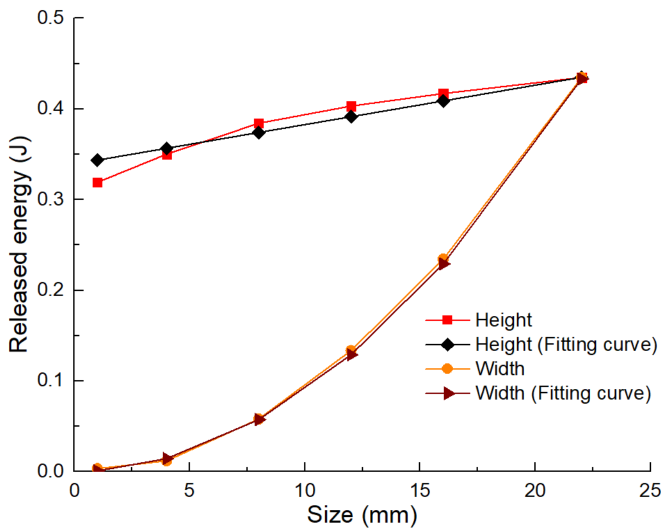

Figure 13. The fitting curve of Equation (9). If the width or height of 22 mm are maintained, then another size changes from 1 mm to 22 mm.

4. Effect of Lateral Pressure on Strain Energy Release

4.1. Model Construction and Results

Due to the influence of the Earth structure motion, the horizontal stress in most areas is higher than the vertical stress. The influence of lateral pressure on strain energy release should be analyzed, and the ratio of horizontal stress σ_x to vertical stress σ_y is defined as the lateral pressure coefficient λ. As shown in Figure 14, in addition to two pressure platens arranged at the upper and lower ends of specimen, another two pressure platens are arranged on the left and right sides of specimen. The load in the vertical direction is Fy, and the load in the horizontal direction is Fx. A positive displacement indicates that the specimen is compressed in this direction, and a negative displacement indicates that the specimen expands in this direction. The size and material parameters of the specimen are consistent with Section 2.3. The rectangle hole of specimen with holes is 22 mm × 22 mm.

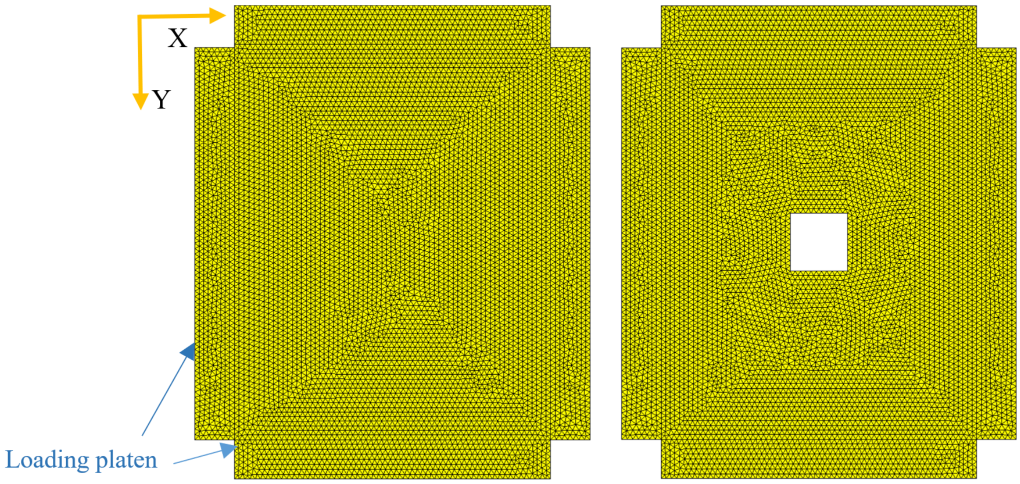

Figure 14. The lateral pressure coefficient λ increases from 0.1 to 1.35 under biaxial loading.

The lateral pressure coefficient is for the intact specimen. The vertical stress should be maintained at 16.9 MPa, then the corresponding horizontal stress is calculated according to the lateral pressure coefficient. Different lateral pressures of intact specimens are achieved by changing the displacement of the pressure platen in the horizontal and vertical directions. Firstly, the intact specimen is loaded, and then the specimen with holes is loaded with the same displacement. The displacement of the specimen with hole is the same as that of the intact specimen in the Y and X directions. The lateral pressure coefficient increases from 0.1 to 1.35.

The displacement and load corresponding to different lateral pressure coefficients are shown in Table 7. As can be seen from Table 7, when the lateral pressure coefficient is 0.1 to 0.4, the displacement Dx in the horizontal direction is negative, which is caused by the expansion in the X direction of the specimen under compression in Y direction. With the increase in lateral pressure coefficient, the displacement in the X direction gradually increases, and the displacement in Y direction gradually decreases. This is because the increase in horizontal stress will lead to an increase in vertical stress caused by the Poisson effect. Therefore, in order to reach the same vertical stress σ_y, it is necessary to reduce the displacement in Y direction. In addition, under the same displacement, the load in the Y direction of the specimen with holes decreases slowly with the increase in the lateral pressure.

Table 7. Displacement and load in vertical and horizontal directions under different lateral pressure coefficients.

λ	Displacment/mm		Intact Specimen				Specimen with Hole	
	Dy	Dx	Fy/kN	Fx/kN	σ_y/MPa	σ_x/MPa	Fy/kN	Fx/kN
0.10	0.431	−0.142	40.56	5.07	16.90	1.69	37.06	3.27
0.25	0.398	−0.088		12.67		4.22	36.93	10.26
0.40	0.365	−0.033		20.28		6.76	36.80	17.26
0.60	0.322	0.039		30.42		10.14	36.66	26.44
0.80	0.277	0.112		40.56		13.52	36.42	35.84
1.00	0.232	0.186		50.70		16.90	36.19	45.24
1.20	0.189	0.257		60.84		20.28	36.05	54.43
1.35	0.156	0.312		68.44		22.82	35.97	61.52

4.2. *Effect of Lateral Pressure*

The strain energy of each part is calculated by Table 7 and Equations (1)–(5), as shown in Table 8 and Figure 15. As shown in Table 8, the strain energy of intact specimens and specimens with holes first decreases and then increases with the increase in lateral pressure coefficient, and the minimum value appears when the lateral pressure coefficient is 0.4–0.6. This is because under the same vertical load, the increase in lateral displacement reduces the displacement in vertical direction, resulting in the decrease in vertical strain energy. When the lateral pressure coefficient is greater than 0.6, the strain energy in the horizontal direction increases exponentially.

Table 8. The strain energy of each part under different lateral pressure coefficients λ.

λ	U_{Int}/J	U_{Hole}/J	$U_{Aft\text{-}ex}$/J	$U_{Spe\text{-}ho}$/J	U_{Rele}/J
0.10	8.38	0.23	8.15	7.76	0.40
0.25	7.51	0.20	7.31	6.90	0.41
0.40	7.07	0.19	6.88	6.43	0.45
0.60	7.12	0.19	6.93	6.42	0.51
0.80	7.89	0.21	7.68	7.05	0.63
1.00	9.42	0.25	9.17	8.41	0.76
1.20	11.65	0.31	11.34	10.40	0.94
1.35	13.84	0.37	13.47	12.40	1.07

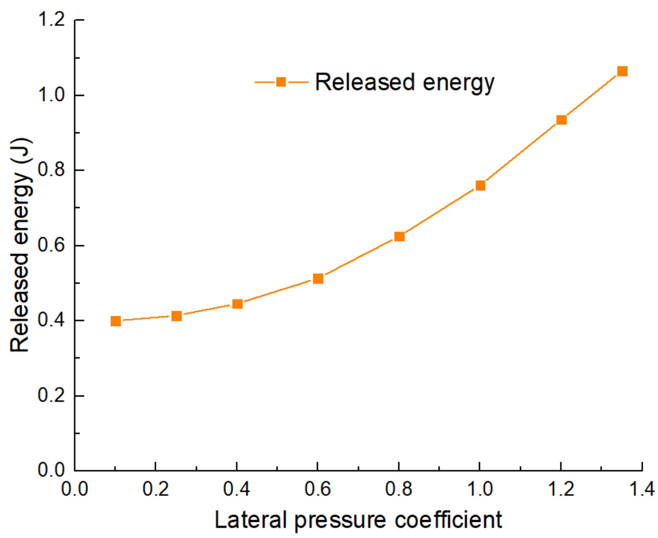

Figure 15. Strain energy release caused by different lateral pressure coefficient λ.

As shown in Figure 15, the strain energy release increases exponentially with the increase in lateral pressure, showing a trend of the second power of lateral pressure coefficient. This shows that the vertical stress remains unchanged, and the increase in horizontal stress will lead to the increase in strain energy release. Similar to the second power shown in Figure 12, this is because the release of strain energy in the horizontal direction is the second power of the horizontal stress, which can be calculated according to Equation (9).

5. Rock Failure Caused by Excavation

5.1. Numerical Method and Model

It is difficult to simulate the excavation in rock mass under high stress through indoor physical experiments, especially the failure process caused by excavation. Fortunately, the numerical analysis method can reproduce the excavation and failure process in rock mass under high stress. The coupled finite and discrete element method (FDEM) is used for the research, and the simulation is carried out by the code ELFEN. The method can realize the real simulation of the brittle failure process of materials by mixing finite and discrete elements and introducing the principle of fracture mechanics [19].

The Mohr–Coulomb criterion with a tension cut-off yield criterion was chosen as the failure criterion of the rock material in this study. Compared with the traditional Mohr-Coulomb criterion, the modified criterion can better describe both the shear and tensile failure of rock material, as shown in Figure 16.

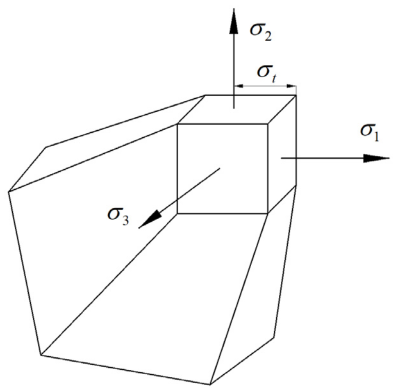

Figure 16. Mohr–Coulomb with tension cut-off yield surface.

The Mohr–Coulomb criterion with a tension cut-off yield criterion combines the Mohr-Coulomb yield criterion and the Rankine tensile yield criterion. The Mohr-Coulomb yield criterion is used to judge shear failure and is described by Equation (10):

$$\tau = c - \sigma_n \tan\varphi \tag{10}$$

where τ is the shear stress, c is the cohesion, σ_n is the normal pressure, and φ is the friction angle.

The Rankine tensile yield criterion is used to judge tensile failure and is described by Equation (11):

$$\sigma_i - \sigma_t = 0 \quad \mathrm{i} = 1,\ 2,\ 3 \tag{11}$$

where σ_i is each principal stress, σ_t is the tensile strength.

The cohesion of material decreases after plastic strain occurs, and the tensile strength is softened by the decrease in cohesion, as shown in Equation (12). This ensures that there is always normal stress on the failure shear surface:

$$\sigma_t \leq c(1 - \sin\varphi)/\cos\varphi \tag{12}$$

The fracture energy G_f is an important parameter for fracture development. For a material, the more energy that is released, the greater the generated crack area. This can be calculated by uniaxial tensile test, and refers to the energy required to generate continuous cracks per unit area. The unit is J/m^2, also written as N/m. It is defined as:

$$G_f = \int \sigma du = \int \sigma \varepsilon(s) ds \tag{13}$$

where σ is the tensile stress, and u is the tensile displacement.

As shown in Figure 17, a model with side length of 20 m is first established. Then, according to the principal stress value of the −720 m buried depth in a mine [14], the maximum horizontal principal stress 33 MPa and vertical principal stress 20 MPa are applied at the boundary of the model, as shown in Equation (14). Finally, a tunnel with a side length of 4 m is excavated in the model center. The material properties are shown in Table 9.

$$\begin{cases} \sigma_H = 0.043h + 1.433 \\ \sigma_v = 0.027h + 0.838 \end{cases} \tag{14}$$

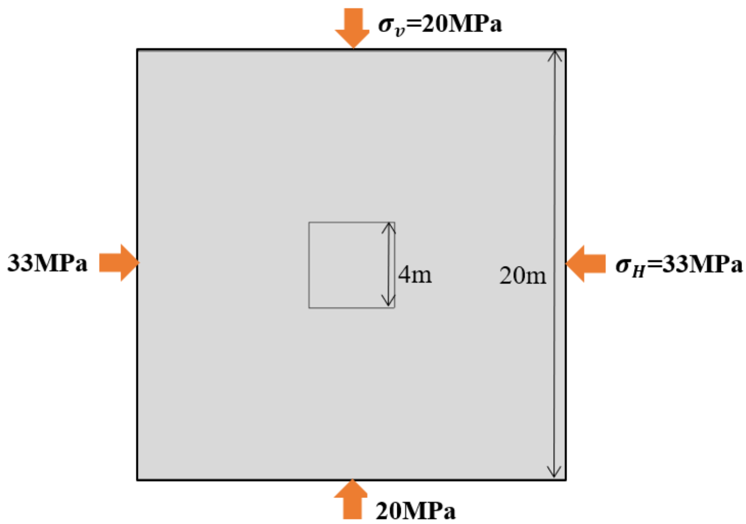

Figure 17. Loading schematic of model.

Table 9. Material properties adopted in model.

Mechanical Parameters	Model
Young's modulus (E, GPa)	20.7
Poisson's ratio (ν)	0.23
Density (ρ, kg/m^3)	2790
Friction angle (φ)	30°
Cohesion (c, MPa)	10
Tensile strength (σ_t, MPa)	2
Fracture energy (G_f, N/m)	4

5.2. Rock Failure Caused by Excavation

As shown in Figure 18, the surrounding rock of the tunnel suffered failure after excavation. The excavation caused tangential stress concentration and normal stress release. It is known that the maximum tangential stress appears at the roof and bottom, which is the reason for the V-shaped rockburst failure of the roof and bottom. In addition, normal stress release caused the tensile spalling failure of the sidewall. Similar damage was also observed in a deep tunnel of a gold mine, as shown in Figure 19.

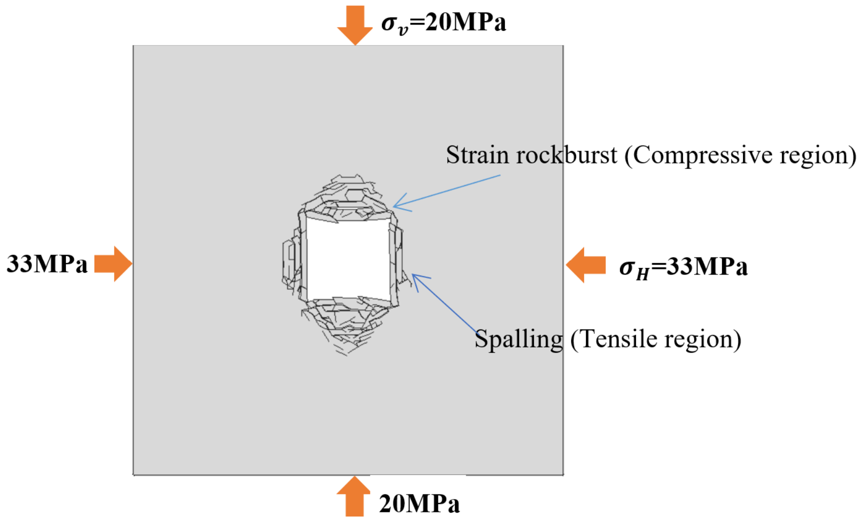

Figure 18. Tunnel failure caused by excavation under pre-stressed state.

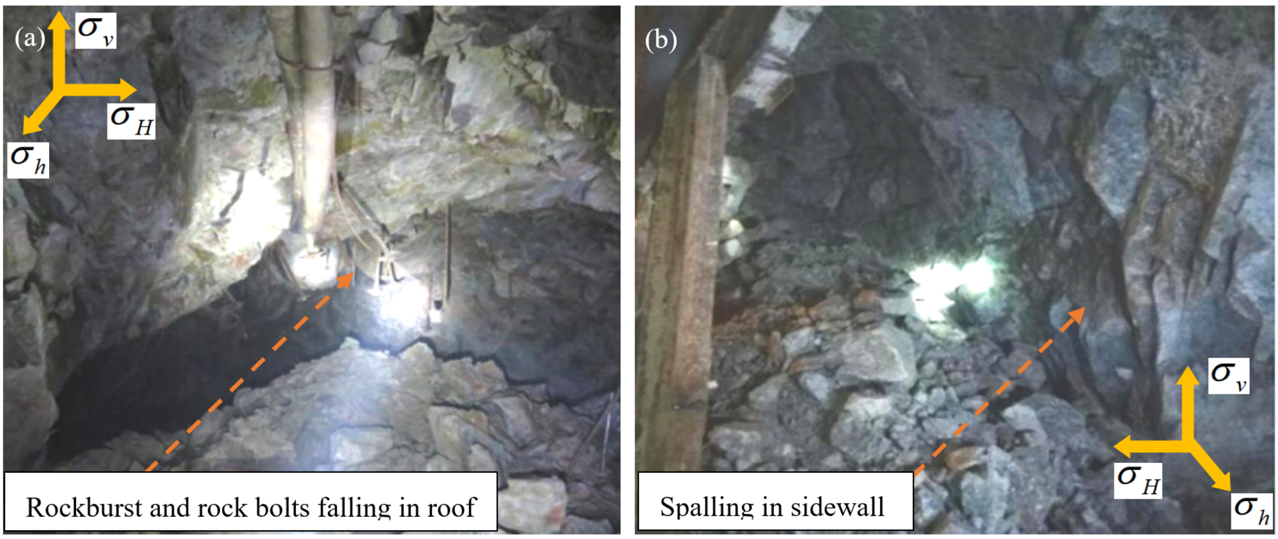

Figure 19. Tunnel failure at buried depth −830 m of a gold mine. (**a**) rockburst and rock bolts falling in roof; (**b**) spalling in sidewall.

Figure 19 shows the tunnel failure with a buried depth −830 m in a gold mine. The principal stresses in three directions are marked in the figure, and the maximum horizontal principal stress is perpendicular to the sidewall. It can be seen that the roof and sidewall are damaged, similar to the failure mode in Figure 18. The rockburst failure in the roof is caused by the concentration of tangential stress, while the spalling failure in the sidewall is caused by the release of normal stress.

6. Conclusions

The main conclusions of this article are listed as follows:

(1) Excavation in pre-stressed rock leads to a change in the original stress field, which is manifested in the release of normal stress on the free surface and the concentration of tangential stress. In this research, a method is proposed to calculate the strain energy release caused by the excavation by loading an intact specimen and a specimen with holes. The energy change in the intact specimen from loading to excavation, and then to stability (stress balance) causes a gradual increase in strain energy during loading, a reduction in strain energy after excavation, and strain energy release after excavation.

Both the excavation and normal stress release after excavation lead to a reduction in strain energy in the rock specimen.

(2) The influence of excavation height and width on strain energy release is inconsistent under vertical loading. When the height of hole is 1 mm, the strain energy release is large, and the increase in the height of the hole will lead to a slow increase in strain energy release. When the width of hole is 1 mm, the strain energy release is very small, and the increase in width of hole will lead to an exponential release of strain energy. Through equation fitting, the theoretical Equation (9) of strain energy release caused by holes with different height and width is obtained, and the fitting accuracy is high.

(3) The strain energy release increases exponentially with the increase in the lateral pressure coefficient, showing a trend of the second power of lateral pressure coefficient. This shows that the vertical stress remains unchanged, and the increase in horizontal stress will lead to the increase in strain energy release.

(4) The tunnel failure mode caused by excavation under high stress is obtained by numerical calculation. The failure modes of the tunnel are strain rockbursts caused by tangential stress concentration and spalling caused by normal stress release, which are also observed in the failure mode of the actual tunnel. For an underground mine exposed to high horizontal stresses, the single excavation height should be reduced to reduce the rate of horizontal strain energy release. In addition, it is recommended that energy-absorbing materials are used to absorb the strain energy release caused by excavation. The support design can be based on the strain energy release of surrounding rock and the amount of energy absorption by the support structure.

Author Contributions: Conceptualization, P.X.; methodology, P.X.; software, P.X.; writing—review and validation, P.X., D.L. and Q.Z.; funding acquisition, D.L. All authors have read and agreed to the published version of the manuscript.

Funding: This research was funded by the National Natural Science Foundation of China (Grant No. 52074349).

Institutional Review Board Statement: Not applicable.

Informed Consent Statement: Not applicable.

Data Availability Statement: The data presented in this study are available on request from the corresponding author.

Conflicts of Interest: The authors declare no conflict of interest.

References

1. Li, X.; Zhou, J.; Wang, S.; Liu, B. Review and practice of deep mining for solid mineral resources. *Chin. J. Nonferrous Met.* **2017**, *27*, 1236–1262.
2. Shi, Q.; Pan, J.; Wang, S.; Liu, S.; Mishra, B.; Seitz, S. Field Monitoring of Delayed Coal Burst in an Advancing Entry of a Deep Coal Mine. *Min. Metall. Explor.* **2021**, *38*, 2417–2431. [CrossRef]
3. Feng, G.-L.; Feng, X.-T.; Xiao, Y.-X.; Yao, Z.-B.; Hu, L.; Niu, W.-J.; Li, T. Characteristic microseismicity during the development process of intermittent rockburst in a deep railway tunnel. *Int. J. Rock Mech. Min. Sci.* **2019**, *124*, 104135. [CrossRef]
4. Lu, M.; Grov, E.; Dahle, H.; Qiao, H.; Wen, B.; Chen, Z.; Zhao, Q. Rock Support Design For Special Lighting Caverns In High In-Situ Stress Rock Mass. *Chin. J. Rock Mech. Eng.* **2008**, *27*, 35–41.
5. Shan, Z.-G.; Yan, P. Management of rock bursts during excavation of the deep tunnels in Jinping II Hydropower Station. *Bull. Eng. Geol. Environ.* **2010**, *69*, 353–363. [CrossRef]
6. Liang, Z.; Xue, R.; Xu, N.; Li, W. Characterizing rockbursts and analysis on frequency-spectrum evolutionary law of rockburst precursor based on microseismic monitoring. *Tunn. Undergr. Space Technol.* **2020**, *105*, 103564. [CrossRef]
7. Li, X.; Gong, F.; Tao, M.; Dong, L.; Du, K.; Ma, C.; Zhou, Z.; Yin, T. Failure mechanism and coupled static-dynamic loading theory in deep hard rock mining: A review. *J. Rock Mech. Geotech. Eng.* **2017**, *9*, 767–782. [CrossRef]
8. Li, C.C.; Mikula, P.; Simser, B.; Hebblewhite, B.; Joughin, W.; Feng, X.; Xu, N. Discussions on rockburst and dynamic ground support in deep mines. *J. Rock Mech. Geotech. Eng.* **2019**, *11*, 1110–1118. [CrossRef]
9. Lu, C.-P.; Liu, Y.; Zhang, N.; Zhao, T.-B.; Wang, H.-Y. In-situ and experimental investigations of rockburst precursor and prevention induced by fault slip. *Int. J. Rock Mech. Min. Sci.* **2018**, *108*, 86–95. [CrossRef]

10. Zhou, J.; Li, X.; Mitri, H.S. Evaluation method of rockburst: State-of-the-art literature review. *Tunn. Undergr. Space Technol.* **2018**, *81*, 632–659. [CrossRef]
11. He, M.; Sousa, R.L.; Müller, A.L.; Vargas, E., Jr.; Sousa, L.R.; Chen, X. Analysis of excessive deformations in tunnels for safety evaluation. *Tunn. Undergr. Space Technol.* **2015**, *45*, 190–202. [CrossRef]
12. Wu, Z.; Wu, S.; Cheng, Z. Discussion and application of a risk assessment method for spalling damage in a deep hard-rock tunnel. *Comput. Geotech.* **2020**, *124*, 103632. [CrossRef]
13. Li, C.C. Principles and methods of rock support for rockburst control. *J. Rock Mech. Geotech. Eng.* **2021**, *13*, 46–59. [CrossRef]
14. Miao, S.; Cai, M.; Guo, Q.; Huang, Z. Rock burst prediction based on in-situ stress and energy accumulation theory. *Int. J. Rock Mech. Min. Sci.* **2016**, *83*, 86–94. [CrossRef]
15. Li, P.; Cai, M.; Guo, Q.; Miao, S. In Situ Stress State of the Northwest Region of the Jiaodong Peninsula, China from Overcoring Stress Measurements in Three Gold Mines. *Rock Mech. Rock Eng.* **2019**, *52*, 4497–4507. [CrossRef]
16. Feng, F.; Li, X.; Rostami, J.; Peng, D.; Li, D.; Du, K. Numerical Investigation of Hard Rock Strength and Fracturing under Polyaxial Compression Based on Mogi-Coulomb Failure Criterion. *Int. J. Geomech.* **2019**, *19*, 04019005. [CrossRef]
17. Zhou, Z.; Li, Z.; Gao, C.; Zhang, D.; Wang, M.; Wei, C.; Bai, S. Peridynamic micro-elastoplastic constitutive model and its application in the failure analysis of rock masses. *Comput. Geotech.* **2021**, *132*, 104037. [CrossRef]
18. Xiao, P.; Li, D.; Zhao, G.; Liu, H. New criterion for the spalling failure of deep rock engineering based on energy release. *Int. J. Rock Mech. Min. Sci.* **2021**, *148*, 104943. [CrossRef]
19. Feng, F.; Li, X.; Rostami, J.; Li, D. Modeling hard rock failure induced by structural planes around deep circular tunnels. *Eng. Fract. Mech.* **2019**, *205*, 152–174. [CrossRef]
20. Wei, C.; Zhang, C.; Canbulat, I.; Huang, W. Numerical investigation into impacts of major fault on coal burst in longwall mining—A case study. *Int. J. Rock Mech. Min. Sci.* **2021**, *147*, 104907. [CrossRef]
21. Gong, F.; Yan, J.; Li, X.; Luo, S. A peak-strength strain energy storage index for rock burst proneness of rock materials. *Int. J. Rock Mech. Min. Sci.* **2019**, *117*, 76–89. [CrossRef]
22. Jiang, Q.; Feng, X.-T.; Xiang, T.-B.; Su, G.-S. Rockburst characteristics and numerical simulation based on a new energy index: A case study of a tunnel at 2500 m depth. *Bull. Eng. Geol. Environ.* **2010**, *69*, 381–388. [CrossRef]
23. Qiu, S.; Feng, X.; Zhang, C.; Xiang, T. Estimation of rockburst wall-rock velocity invoked by slab flexure sources in deep tunnels. *Can. Geotech. J.* **2014**, *51*, 520–539. [CrossRef]
24. He, B.-G.; Zelig, R.; Hatzor, Y.H.; Feng, X.-T. Rockburst Generation in Discontinuous Rock Masses. *Rock Mech. Rock Eng.* **2016**, *49*, 4103–4124. [CrossRef]
25. Xiao, P.; Li, D.; Zhao, G.; Zhu, Q.; Liu, H.; Zhang, C. Mechanical properties and failure behavior of rock with different flaw inclinations under coupled static and dynamic loads. *J. Cent. South Univ.* **2020**, *27*, 2945–2958. [CrossRef]
26. Qiu, J.; Li, X.; Li, D.; Zhao, Y.; Hu, C.; Liang, L. Physical Model Test on the Deformation Behavior of an Underground Tunnel Under Blasting Disturbance. *Rock Mech. Rock Eng.* **2021**, *54*, 91–108. [CrossRef]
27. Zhou, Z.; Cai, X.; Li, X.; Cao, W.; Du, X. Dynamic Response and Energy Evolution of Sandstone Under Coupled Static-Dynamic Compression: Insights from Experimental Study into Deep Rock Engineering Applications. *Rock Mech. Rock Eng.* **2020**, *53*, 1305–1331. [CrossRef]
28. Han, Z.; Li, D.; Zhou, T.; Zhu, Q.; Ranjith, P.G. Experimental study of stress wave propagation and energy characteristics across rock specimens containing cemented mortar joint with various thicknesses. *Int. J. Rock Mech. Min. Sci.* **2020**, *131*, 104352. [CrossRef]
29. Skrzypkowski, K. Case Studies of Rock Bolt Support Loads and Rock Mass Monitoring for the Room and Pillar Method in the Legnica-Gogow Copper District in Poland. *Energies* **2020**, *13*, 2998. [CrossRef]
30. Jiang, J.; Su, G.; Zhang, X.; Feng, X.-T. Effect of initial damage on remotely triggered rockburst in granite: An experimental study. *Bull. Eng. Geol. Environ.* **2020**, *79*, 3175–3194. [CrossRef]
31. Chen, G.; He, M.; Fan, F. Rock Burst Analysis Using DDA Numerical Simulation. *Int. J. Geomech.* **2018**, *18*, 04018001. [CrossRef]
32. Lin, M.-Q.; Zhang, L.; Liu, X.-Q.; Xia, Y.-Y.; Zhang, D.-J.; Peng, Y.-L. Microscopic analysis of rockburst failure on specimens under gradient stress. *Rock Soil Mech.* **2020**, *41*, 2984–2992.
33. Rui, Y.; Zhou, Z.; Lu, J. A novel AE source localization method using clustering detection to eliminate abnormal arrivals. *Int. J. Min. Sci. Technol.* **2022**, *32*, 51–62. [CrossRef]
34. Xiao, P.; Li, D.; Zhao, G.; Liu, M. Experimental and Numerical Analysis of Mode I Fracture Process of Rock by Semi-Circular Bend Specimen. *Mathematics* **2021**, *9*, 1769. [CrossRef]
35. Read, R. 20 years of excavation response studies at AECL's Underground Research Laboratory. *Int. J. Rock Mech. Min. Sci.* **2004**, *41*, 1251–1275. [CrossRef]
36. Kang, S.S.; Ishiguro, Y.; Obara, Y. Evaluation of core disking rock stress and tensile strength via the compact conical-ended borehole overcoring technique. *Int. J. Rock Mech. Min. Sci.* **2006**, *43*, 1226–1240. [CrossRef]
37. Hu, X.; Su, G.; Chen, G.; Mei, S.; Feng, X.; Mei, G.; Huang, X. Experiment on Rockburst Process of Borehole and Its Acoustic Emission Characteristics. *Rock Mech. Rock Eng.* **2019**, *52*, 783–802. [CrossRef]
38. Gong, F.; Wu, W.; Li, T.; Si, X. Experimental simulation and investigation of spalling failure of rectangular tunnel under different three-dimensional stress states. *Int. J. Rock Mech. Min. Sci.* **2019**, *122*, 104081. [CrossRef]

39. Qiu, P.-Q.; Ning, J.-G.; Wang, J.; Hu, S.-C.; Li, Z. Mitigating rock burst hazard in deep coal mines insight from dredging concentrated stress: A case study. *Tunn. Undergr. Space Technol.* **2021**, *115*, 104060. [CrossRef]
40. Tao, M.; Li, X.; Li, D. Rock failure induced by dynamic unloading under 3D stress state. *Theor. Appl. Fract. Mech.* **2013**, *65*, 47–54. [CrossRef]
41. Feng, F.; Li, X.; Luo, L.; Zhao, X.; Chen, S.; Jiang, N.; Huang, W.; Wang, Y. Rockburst response in hard rock owing to excavation unloading of twin tunnels at great depth. *Bull. Eng. Geol. Environ.* **2021**, *80*, 7613–7631. [CrossRef]
42. Ren, F.; Chang, Y.; He, M. A systematic analysis method for rock failure mechanism under stress unloading conditions: A case of rock burst. *Environ. Earth Sci.* **2020**, *79*, 370. [CrossRef]
43. Huang, R.Q.; Wang, X.N.; Chan, L.S. Triaxial unloading test of rocks and its implication for rock burst. *Bull. Eng. Geol. Environ.* **2001**, *60*, 37–41. [CrossRef]
44. Su, G.; Hu, L.; Feng, X.; Wang, J.; Zhang, X. True triaxial experimental study of rockburst process under low frequency cyclic disturbance load combined with static load. *Chin. J. Rock Mech. Eng.* **2016**, *35*, 1309–1322.